Macromolecules

Article

Cite This: Macromolecules 2018, 51, 10285−10296

pubs.acs.org/Macromolecules

Kinetics and Energetics of Solute Segregation in Granular Block Copolymer Microstructures

Bongjoon Lee,[†] Markus Bleuel,[§,∥] Adrian Zhao,[†] David Ott,[†] Ilhem F. Hakem,[‡] and Michael R. Bockstaller*[,†]

[†]Department of Materials Science and Engineering and [‡]Department of Chemical Engineering, Carnegie Mellon University, 5000 Forbes Ave., Pittsburgh, Pennsylvania 15213, United States

[§]NIST Center for Neutron Research, National Institute of Standards and Technology, Gaithersburg, Maryland 20988-8562, United States

[∥]Department of Materials Science and Engineering, University of Maryland, College Park, Maryland 20742-2115, United States

Supporting Information

ABSTRACT: The segregation kinetics of deuterated polystyrene (d-PS) within the grain boundary regions of a lamellar poly(styrene-*b*-isoprene) copolymer is analyzed using a combination of electron imaging and grain mapping as well as ultrasmall and small-angle neutron scattering. Solute segregation is limited to high-angle grain boundaries (that is, boundaries between grains having misorientations that exceed a threshold value). The accumulation of d-PS is found to be uniform across high-angle boundaries, reaching an equilibrium local concentration of solute within the boundary regions of about 52 vol %. This is interpreted as a consequence of d-PS segregation enabling the relaxation of perturbed chain conformations in the boundary regions, thus reducing the elastic strain energy that is stored in high-angle boundaries. The elastic strain energy is estimated using a continuum layer deformation model and compared to the experimental (relative) boundary tension that is determined by analysis of dihedral angles at grain boundary triple junctions. A McLean-type interface adsorption model is demonstrated to quantitatively capture both the kinetics and the extent of solute accumulation within boundary regions. The model reveals that the rate of segregation is sensitive to the mobility of the solute while the limiting concentration of solute within high-angle boundaries is determined by the energy of grain boundary defects. The results provide a basis for the interpretation of structure coarsening processes in block copolymer blend systems that are often found to result in more granular microstructures (featuring smaller grain sizes) as compared to the pristine block copolymer analogues and inform the development of processes for the strategic decoration of defects to enable new functionalities in block copolymer-based materials.

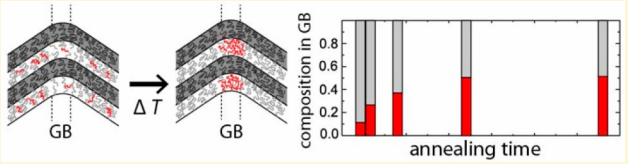

INTRODUCTION

The ability to organize into periodic microdomain structures has rendered block copolymer (BCP)-based materials candidates for innovative material technologies in areas such as photonics, energy storage, or photovoltaics.[1−10] In applications such as these, large-grained microstructures are often preferred, and hence the development of "alignment methods" to enable the fabrication of microstructures with reduced defect densities continues to be a relevant area of BCP research.[11−13] While for thin films the applications of electric, magnetic, or mechanical fields, thermal field gradients, and chemo- and graphoepitaxy have been shown to effectively guide structure formation depending on the material composition, these methods typically are not practical to align materials in the bulk state.[13−22] Hence, for bulk BCPs, the "engineering" of the grain structure is often limited to the application of thermal annealing to induce grain coarsening. The kinetics of grain growth will, in general, depend on material characteristics (such as chain dynamics and the presence of entanglements) as well the energetic and kinetic parameters of microstructural reorganization. Understanding of the mechanism of grain growth and the evolution of grain boundary (GB) defect structures during thermal (or solvent) annealing is therefore a subject that is of fundamental relevance to both the science and engineering of BCP-based materials.

The mechanism of morphology evolution in BCP and BCP-blend materials has been the subject of extensive research during the past 20 years, however, mostly with focus on the nucleation and growth process during the early state of microphase separation.[23−34] Pioneering work on the characterization of GB defects by the Thomas and Hashimoto groups established the distinct types of GB structures in lamellar BCP microstructures: twist (helicoid and Scherk surface) and tilt (chevron, omega, and T-junction) boundary morphologies.[35−40] Insight into the energetics of GB defects was first provided by numerical simulations that revealed the energy of

Received: September 21, 2018
Revised: December 1, 2018
Published: December 14, 2018

DOI: 10.1021/acs.macromol.8b02044
Macromolecules 2018, 51, 10285−10296

GB defects to sensitively depend on the GB type as well as the misorientation between grains.[41,42] The results further suggested that the frequency of grain misorientations in quiescent organized BCP microstructures follows a Boltzmann distribution. Both predictions were experimentally validated by Ryu et al. using triple-junction analysis.[43] Numerical studies also were the first to suggest that—in block copolymer/homopolymer (BCP/hP) blends—the segregation of hP solute within GB regions can reduce the energy of GB defects.[42] The first experimental results to provide indirect support for this hypothesis were provided by Burgaz et al., who attributed the higher frequencies of T-junction grain boundaries in block copolymer blends to the reduction of the energy penalty associated with defect formation.[44] It has since been shown that the interaction of "solute species" with GB defects is a general phenomenon that is also relevant to nanoparticle or smaller molecular additives.[45,46]

While these previous studies have established the foundation to interpret *individual* defect structures in BCP materials, much less is known about the relationship between statistical representations of microstructural characteristics and the coarsening of BCPs during microstructure annealing. In two previous papers (that we will refer to in the following as "Grain Coarsening-I" and "Grain Coarsening-II"), we established the grain coarsening characteristics in a lamellar poly(styrene-*b*-isoprene) (PS−PI) model system.[47,48] A procedure involving stereological analysis of large area electron micrographs (using serial imaging, reconstruction, and pattern matching and filtering) was developed to evaluate the evolution of grain size, orientation, and grain boundary structures during thermal annealing of bulk films. Grain growth in the PS−PI test system was found to proceed via the initial relaxation of "frozen-in" kink boundary defects and the subsequent continuous grain growth by relaxation of symmetric tilt GBs.[47] The grain growth kinetics was found to be consistent with normal grain growth (as indicated by a grain growth exponent $n \cong 1.8$), thus suggesting that grain growth in BCPs—just as in metals or ceramics—is driven by the reduction of the surface energy stored in GB interfaces.[47] The addition of PS homopolymer was shown to reduce the growth rate in PS−PI/PS films; for PS−PI blended with 10 wt % PS *stagnation of grain growth* was observed after short annealing periods.[48] The stagnation effect was rationalized as a consequence of the segregation of PS homopolymer into GB regions. This was argued to reduce the energy of boundary defects and thus the driving pressure for grain growth.[48]

The stagnation of grain growth due to additives highlights a profound challenge for the fabrication of large-grained microstructures in blended BCP systems. For example, the success of alignment methods would be expected to depend on the balance between the dynamics of microstructure alignment and the kinetics (and extent) of solute segregation. The purpose of the present contribution is to evaluate the role of GB characteristics on both the rate of homopolymer segregation and the limiting concentration of solute within GB regions in a PS−PI/PS model system during thermal annealing. The results reveal that homopolymer segregation occurs during the early stage of thermal annealing and that the distribution of solute is approximately uniform across GBs exceeding a threshold misorientation $\theta \sim 60°$, reaching a final volume fraction of PS within the GB of about 0.52. The segregation kinetics is quantitatively described by a Langmuir−McLean type isotherm model. This supports the conclusion that segregation is driven by the associated release of elastic energy that is stored in high-angle GB regions.

The structure of the paper is as follows: First, we outline the process involving combined grain mapping analysis as well as small- and ultrasmall-angle neutron scattering to determine the homopolymer concentration within grain boundary structures during thermal annealing of the PS−PI/PS blend system. The results of grain mapping analysis will be presented to establish the relevant morphological parameters (such as grains size, grain size distribution, misorientation of grain boundary interfaces, and relative grain boundary energy) that motivate the assumptions underlying the neutron scattering analysis. Subsequently, ultrasmall-angle neutron scattering will be used to quantitatively determine the concentration of homopolymer solute within grain boundary regions. In the final part of the paper we will present a statistical model to rationalize the experimental trend of solute segregation.

MATERIALS AND METHODS

Materials. Poly(styrene-*b*-isoprene) (PS−PI) with molecular weight M_w = 91 kg/mol (45 kg/mol-*b*-46 kg/mol), molecular weight dispersity index M_w/M_n = 1.07, and volume fraction of polystyrene component ϕ_{PS} = 0.46 was purchased from Polymer Source. The degree of segregation is estimated to χN = 57 at the annealing temperature (T = 130 °C), where χ is the Flory−Huggins parameter and N is the degree of polymerization. Fully deuterated polystyrene (PS-d_8, in the following abbreviated as d-PS) with molecular weight M_w = 20 kg/mol and molecular weight dispersity index M_w/M_n = 1.08 was also purchased from Polymer Source. Toluene (HPLC grade) was purchased from Sigma-Aldrich. All materials were used as received without further purification. PS-grafted gold nanocrystals (AuPS) were synthesized following previously published procedures.[47,48] The particle core diameter of AuPS particles was determined to be d_{Au} = 3 nm by electron microscopy; the molecular weight of grafted polystyrene was 11.5 kg/mol.

Film Preparation. PS−PI film with a deuterated polystyrene weight fraction of 10 wt % was prepared by dissolution of appropriate amounts of homo- and copolymer in toluene (concentration 5 wt %). Using densities for the individual polymer systems of ρ_{PI} = 0.92 g/cm^3, ρ_{PS} = 1.04 g/cm^3, and $\rho_{d\text{-}PS}$ = 1.12 g/cm^3 results in a d-PS volume fraction of 0.088 in the final films. Films of ∼350 μm thickness were cast at T = 23 °C at a partial pressure of toluene of p = 80 mbar (pressure was controlled using a modified Büchi Rotavapor R-200); the time for solvent evaporation was 8 h. Samples were thermally annealed under vacuum at 130 °C for 0, 3, 24, 72, and 168 h. PS−PI/AuPS as well as PS−PI/d-PS blends were prepared by mixing of appropriate amounts of material to result in a final concentration of 5 wt % solute in toluene solution and subsequent solvent evaporation at 80 mbar (see above).

Transmission Electron Microscopy (TEM). Electron imaging of BCP microstructures was performed using a JEOL 2000 FX electron microscope operated at 200 kV. Imaging was based on the amplitude and phase contrast, and images were recorded by a Gatan Orius SC600 high-resolution camera. Prior to electron imaging, films were cryo-microtomed at −120 °C using a LEICA EM FCS cryo-ultramicrotome and stained with OsO_4 (selective staining of PI domains) that was obtained from EM Sciences. PS−PI/AuPS films were imaged without further staining.

Microstructure Analysis. Analysis of the grain characteristics as well as type and frequency of grain boundary defects was performed by image analysis following a procedure that has been described in detail in Grain Coarsening-I.[47] Analysis of the relative energies of boundary defects in block copolymers and their blends was performed by analysis of dihedral angles as described in Grain Coarsening-II.[48]

Differential Scanning Calorimetry (DSC). DSC measurements were performed using a TA Instruments DSC 250 with ramping rate of 10 °C/min. Sample amounts of ∼7 mg were placed in a Tzero aluminum pan, and nitrogen gas was purged during measurement.

DOI: 10.1021/acs.macromol.8b02044
Macromolecules 2018, 51, 10285−10296

The measurement was performed four times, and the results have shown good reproducibility.

Ultrasmall/Small-Angle Neutron Scattering (USANS/SANS). USANS and SANS were performed at NCNR (NIST Center for Neutron Research, Gaithersburg, MD). The BT5 USANS instrument covers a q-range between 3×10^{-5} and 2.5×10^{-3} Å^{-1} with neutron wavelength $\lambda = 2.4$ Å and $\Delta\lambda/\lambda = 6\%$ (where q denotes the scattering vector). The NGB-30m SANS instrument covers a q-range between 0.001 and 0.6 Å^{-1} using standard three detector geometries (1 m with an 0.25 m detector offset, 4 m, and 13 m) with $\lambda = 6$ Å neutrons and the neutron lens setting at 8.13 Å neutron wavelength with a wavelength spread of $\Delta\lambda/\lambda = 14\%$. USANS and SANS experiments were performed separately on each beamline, and the data were subsequently combined for invariant analysis. The data reduction was performed using software based on IGOR Pro that was provided by NIST.[49−51] To apply invariant analysis (which assumes the presence of two phases with uniform scattering length density in each), the scattering arising from thermal concentration fluctuations of d-PS within the PS host domains was corrected for the effect of thermal concentration fluctuations. The details of the background correction process are provided in the Supporting Information.

RESULTS AND DISCUSSION

The material system of this study is based on the PS−PI block copolymer that also served as model system in our previous studies.[47,48] The copolymer has a molecular weight of $M_w = 91$ kg/mol with a near symmetric composition ($M_{w,PS} = 45$ kg/mol, $M_{w,PI} = 46$ kg/mol, PS volume fraction $\phi_{PS} \sim 0.46$) and thus forms a lamellar microstructure. The PS−PI is in the intermediate segregation regime with a degree of segregation $\chi N \sim 57$ at the annealing temperature ($T = 130$ °C).[52] To enable the characterization of microstructure evolution via neutron scattering, fully deuterated PS (d-PS) with $M_{w,d\text{-}PS} = 20$ kg/mol was used as a solute. This molecular weight was chosen to enable the miscibility of the solute within the BCP host domain (which generally requires the molecular weight of the homopolymer to be less than of the corresponding block) and to be comparable to the molecular weight of the hydrogenous PS (h-PS) that was used in Grain-Coarsening-II.[48] Similar to the h-PS analogue, full dispersion of the d-PS within the host BCP was observed up to volume fractions of 0.2 with no discernible indication of macrophase separation or order−order transition (results not shown here). Because of the similar miscibility characteristics of h-PS and d-PS solutes, both systems will in the following be assumed to be athermal; thus, any effect of isotopic labeling on the interaction between PS-host domain and d-PS will be neglected. For microstructure analysis, a concentration of 10 wt % d-PS within PS−PI was used. This concentration was chosen for three reasons: First, the analogous amount of solute was previously demonstrated to induce grain stagnation in the PS−PI matrix (Grain Coarsening-II); second, this concentration was found to provide sufficient scattering contrast to enable the characterization of solute segregation using neutron scattering; and third, to ensure that the system remains within the lamellar regime for all tested experimental conditions.

The kinetics of solute segregation was evaluated using a combination of small- and ultrasmall-angle neutron scattering (SANS/USANS) and grain boundary mapping. The approach takes advantage of the significantly different scattering lengths of ^{1}H and ^{2}H isotopes ($b_{1H,coh} = -3.7406$ fm, $b_{1H,incoh} = 25.274$ fm, $b_{2H,coh} = 6.671$ fm, and $b_{2H,incoh} = 4.04$ fm, where $b_{i,coh}$ and $b_{i,incoh}$ represent the coherent and incoherent scattering length of species i, respectively) that result in a scattering length density (SLD) of d-PS that significantly exceeds the SLD of the hydrogenous PS−PI matrix.[53] Specifically, assuming a mass density of $\rho_{h\text{-}PS} = 1.04$ g/cm^3, $\rho_{d\text{-}PS} = 1.12$ g/cm^3, and $\rho_{h\text{-}PI} = 0.92$ g/cm^3 for h-PS, d-PS, and PI, respectively, the scattering length density of the individual components follows as $SLD_{h\text{-}PS} = 1.40 \times 10^{-6}$ Å^2, $SLD_{h\text{-}PI} = 2.70 \times 10^{-7}$ Å^2, and $SLD_{d\text{-}PS} = 6.41 \times 10^{-6}$ Å^2. Because scattering in the ultrasmall-angle range is attributable to SLD heterogeneities on the micrometer scale (i.e., comparable to the size of grains), USANS scattering can be assumed to arise predominantly due to the scattering of the grain boundary regions that are enriched with d-PS solute. The scattering data can thus be interpreted on the basis of a two-phase material consisting of a matrix with "smaller" SLD that is constituted of the PS−PI lamellar structure with small amount of uniformly distributed d-PS (the lamellar fine structure is not "visible" in the USANS range) and the grain boundary regions that are enriched with d-PS solute and thus exhibit a "larger" SLD. The scattering contrast between matrix and boundary regions can be described based on the scattering relation of a general two-phase material as

$$(\Delta SLD)^2 = (SLD_{HAGB} - SLD_m)^2 = \frac{1}{2\pi^2}\frac{1}{\phi_{HAGB}(1-\phi_{HAGB})}\int_0^\infty I(q)q^2\,dq \quad (1)$$

where ϕ_{HAGB} is the volume fraction of grain boundary regions that are decorated with d-PS solute, $I(q)$ is the scattering intensity at scattering vector (modulus) q, SLD_{HAGB} denotes the scattering length density of the decorated GB regions, and SLD_m is the scattering length density of the grain interior (i.e., the average SLD of PS−PI/d-PS).[50] The last term in eq 1 is related to the scattering invariant Q via $\int q^2 I(q)\,dq = (4\pi)^{-1}Q$. If ϕ_{HAGB} is known, for example, through grain mapping analysis, then the scattering contrast and thus composition of GB regions can be determined. We note that the use of the subscript "HAGB" is motivated from the observation that solute segregation is limited to high-angle GB defects (see the following discussion). The structural model that underlies the scattering analysis is illustrated in Figure 1.

As indicated in Figure 1, not every GB is expected to be decorated with d-PS, but only those GBs having a grain misorientation angle that exceeds a threshold value, θ_{crit}, will induce solute sequestration. This was first proposed by Listak et al., who argued that for solute segregation to occur, the release of stored elastic strain energy upon segregation has to outweigh the energy cost associated with the entropy loss due to concentration of the solute within the boundary region.[54] Because the stored elastic strain energy increases with misorientation, so does the propensity of GBs to induce solute segregation. Boundaries with a grain misorientation angle exceeding the threshold for solute segregation will in the following be denoted "high-angle grain boundaries (HAGB)". Because not all grains are bounded by high-angle boundaries, the scattering of PS−PI/d-PS blends in the USANS regime cannot be directly related to grain size but rather will be interpreted in terms of a general two-phase structure via eq 1. This is a difference to earlier studies by Cohen and co-workers, who applied ultrasmall-angle X-ray scattering to determine the average grain size in lamellar BCPs.[55]

To determine the threshold misorientation for solute sequestration, the structure of GBs was analyzed in a PS−PI blended with corresponding amounts of PS-tethered gold nanocrystals. This approach was first used by Listak et al. to analyze the role of misorientation on solute segregation.[54] The

DOI: 10.1021/acs.macromol.8b02044
Macromolecules 2018, 51, 10285−10296

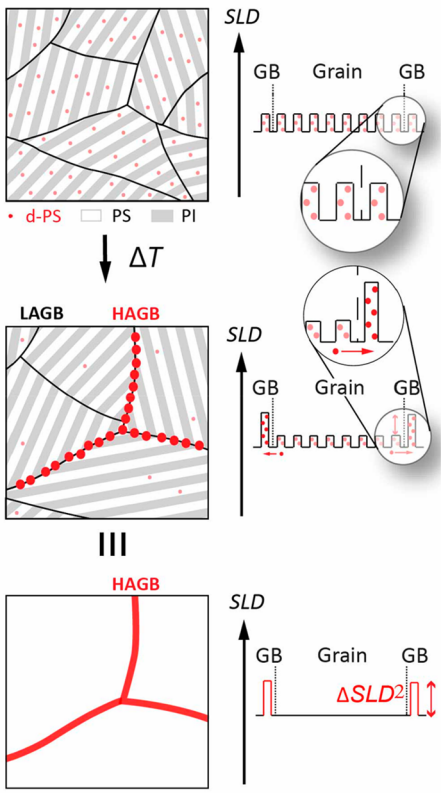

Figure 1. Illustration of model used to quantify solute segregation using USANS. Panels on the left illustrate microstructure (d-PS is highlighted in red). Panels on right show schematic representation of the proposed scattering length density across the grain and grain boundary for as-cast and annealed systems. The top figure illustrates microstructure before thermal annealing. d-PS solute is uniformly distributed across grain. Thermal annealing causes the segregation of d-PS into high-angle grain boundary (HAGB) regions along with increase of SLD. Low-angle grain boundaries (LAGB) are not affected by solute segregation (this will be shown in the discussion below). The figure on the bottom shows the simplified two-phase system of annealed systems that is the basis for the interpretation of ultrasmall-angle scattering data.

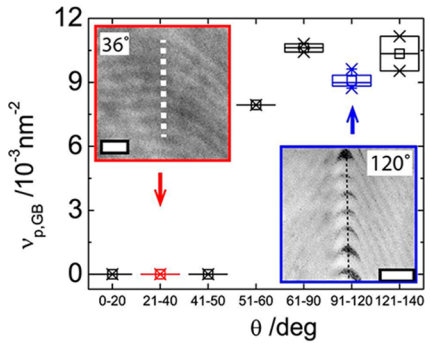

Figure 2. Box plot showing the distribution of the number of particles $\nu_{p,GB}$ within (near-symmetric) GBs as a function of tilt angle after thermal annealing of PS−PI/AuPS blends after 3 days of annealing at T = 130 °C. Particle segregation was observed for tilt angles exceeding a threshold value $\theta > 55°$. Insets display representative transmission electron micrographs of (near-symmetric) tilt GBs with misorientation angles θ = 36° (red) and 120° (blue). The grain boundaries are indicated with dotted lines. AuPS nanoparticles are uniformly dispersed at θ = 36° while segregation occurs for θ = 120°. Scale bars are 200 nm.

authors observed that appropriately modified, small nanocrystals undergo grain segregation similar to homopolymer solutes and can thus be used as "tracer inclusions" to evaluate solute segregation. The threshold angle for HAGBs can then be determined by evaluating the aggregation of particle fillers within GB regions of varied misorientation before and after annealing of the film for 72 h at T = 130 °C. Gold was chosen as a model system because of its high electron density and the availability of established synthetic procedures for surface modification. PS-tethered gold nanocrystals with an average particle diameter $\langle d_{Au} \rangle$ = 3 nm were synthesized using a modified Brust−Schiffrin method.[56−58] The molecular weight of PS ligands was 11.5 kg/mol, and the grafting density was determined (by TGA analysis) to be about 1.1 nm^{-2}, which corresponds approximately to the specifications of particles systems that were previously used by our group.[54] The miscibility of AuPS particles within the PS host domain was confirmed prior to annealing by validating the absence of particle aggregates in large area electron micrographs of PS−PI/AuPS blends prior to annealing (results not shown here). The influence of GB misorientation on particle segregation is illustrated in Figure 2 which depicts the distribution of the number of particles per aggregate within grain boundary regions as a function of tilt angle for near-symmetric tilt grain boundaries (a total of 107 GBs was analyzed). Symmetric tilt GBs were chosen as a reference because this boundary type constitutes the large majority of GBs within lamellar BCP microstructures.[59−61] The figure reveals that particle segregation within GBs exhibits a rather sharp transition within the range of tilt angles from θ = 51° to 60°. Based on the data shown in Figure 2, the threshold misorientation angle for HAGBs is thus defined as θ_{crit} = 60°. Interestingly, the number of particles that segregate within HAGB regions shows only a weak dependence on the misorientation angle; an approximately equal number is observed for GBs with misorientation angles in the range 61°−140°. This trend is consistent with the corresponding trend of GB energy with grain misorientation that has been found to level off at misorientation angles above about 80° due to a transition of the GB structure from Chevron to Omega-type (see Grain Coarsening-II).[48]

We note that the approximately constant number of particles that are segregated within HAGBs motivates and supports an important assumption that underlies the subsequent analysis of USANS data; i.e., the concentration of d-PS within HAGBs (and hence the respective SLD_{HAGB}) is assumed to be uniform across all HAGBs independent of grain misorientation.

To relate the total area of HAGB interfaces (which is measured through grain mapping analysis) to the volume fraction of solute within GB regions (which is measured through neutron scattering via the parameter SLD_{HAGB} in eq 1), the width W of GB regions has to be known. For symmetric tilt boundaries, W is related to the misorientation via $W = 2R/\sin(\theta/2)$, where R denotes the curvature radius of the boundary. The latter can be determined from electron micrographs of tilt GBs. Figure 3 illustrates the geometric analysis of tilt GBs from electron micrographs along with the corresponding values of the normalized GB width W/L (where L = 72 nm represents the lamellar thickness) as a function of misorientation for as-cast PS−PI/d-PS. The figure reveals that the GB width is approximately constant with $W/L \sim 1 \pm 0.15$ independent of grain misorientation. This confirms previous reports, for example, by Gido et al., who reported the GB

DOI: 10.1021/acs.macromol.8b02044
Macromolecules 2018, 51, 10285−10296

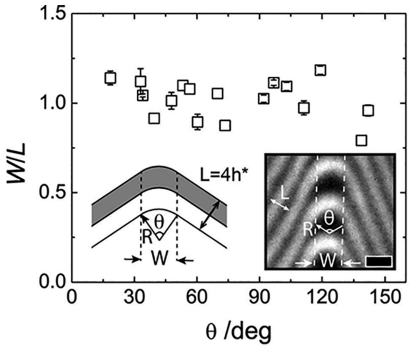

Figure 3. Normalized boundary width W/L (normalized with respect to the unperturbed lamellar spacing L = 72 nm) as a function of tilt angle for PS−PI/d-PS in the as-cast state. The inset shows an illustration of a symmetric tilt (Chevron) boundary morphology. The tilt angle, θ, the radius of curvature, R, and the boundary width, W, are indicated. An example of the analysis for a θ = 114° tilt boundary is shown in the TEM image shown in the inset. The scale bar is 50 nm.

width to be equal to the lamellar spacing.[61] Analogous observations were made for particle-filled as well as pristine PS−PI (see Grain Coarsening-II). Figure 3 hence justifies the assumption that the width of HAGB regions is uniform and equal to L. This allows to assign a volume $A_{HAGB}L$ (where A_{HAGB} denotes the total area associated with HAGBs) to the GB regions that are available for solute segregation in PS−PI/d-PS microstructures. If the volume fraction ϕ_{HAGB} of high angle boundary regions within the microstructure is known, then SLD_{HAGB} (and hence the volume fraction of segregated solute) can be determined from eq 1. This strategy will be used below to quantify the extent and kinetics of solute segregation.

Grain mapping analysis was performed to determine A_{HAGB} as well as other morphological parameters such as average grain size, grain size distribution, grain shape, distribution of misorientation angles of symmetric tilt boundaries, and relative GB energy as a function of tilt angle. The process for grain mapping analysis involves computer-based image reconstruction and processing as well as stereological analysis of large area micrographs and has been detailed in Grain Coarsening-I.[47] Figure 4 depicts a representative grain map of PS−PI/d-PS

Figure 4. Grain map representing microstructure of PS−PI/d-PS (10 wt %) annealed at 130 °C for 3 days. Random (gradient) color assignment is used to distinguish adjacent grains with misorientation exceeding 15°); the x- and y-axes represent the in-plane and out-of-plane (i.e., normal to substrate) orientation of the film. HAGBs with misorientation angle θ > 60° are highlighted with thick black lines.

after 72 h of thermal annealing at T = 130 °C. Adjacent lamellae regions with a misorientation exceeding 15° are differentiated as "separate grains" and identified by random color assignment. Highlighted in bold lines are HAGBs that separate grains with misorientation $\theta \geq 60°$. In the figure, the x-axis denotes the in-plane direction parallel to sample/substrate interface and the y-axis is the out-of-plane direction perpendicular to the sample/substrate interface.

The grain map reveals a distinctive alignment of HAGBs parallel to the in-plane direction of the substrate. This is consistent with previous findings in Grain Coarsening-I where the orientation of HAGBs in-plane direction was attributed to in-plane stresses acting on the film during the late stages of solvent evaporation.[47] From the grain maps of as-cast and thermal annealed samples, the evolution of the grain microstructure during thermal annealing can be evaluated. For example, Figure 5a depicts the evolution of the number-

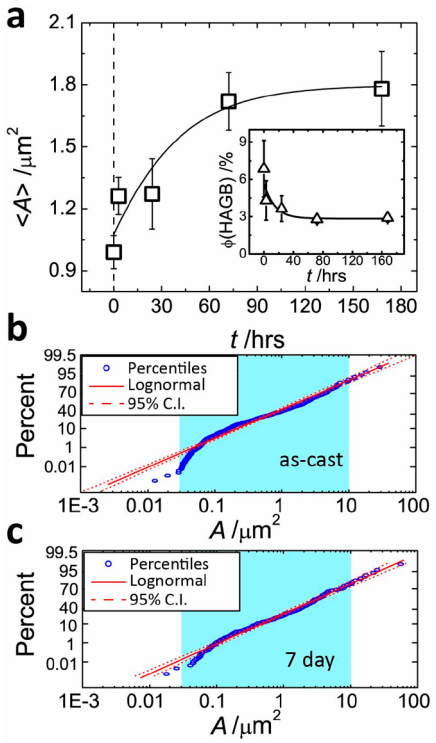

Figure 5. (a) Evolution of number-averaged grain cross-sectional area $\langle A(t) \rangle$ for the PS−PI/d-PS 10 wt % blend system. The grain size increases with thermal annealing time, and the rate of grain growth decreases with annealing time. Error bars correspond to one standard deviation. Inset shows plot of volume fraction of HAGB (θ > 60°) as a function of thermal annealing time. The volume fraction decreases exponentially with thermal annealing time and remains constant after about 20 h of annealing. (b) and (c) show log-normal probability plots representing grain size distribution for as-cast (t = 0 h) and after 7 days (t = 144 h) of thermal annealing. The middle red solid lines of each plot indicate log-normal distribution; the two dotted lines represent the 95% confidence intervals. Blue shaded areas delineate the range of grain sizes that was considered for grain structure analysis (see ref 47 for more information about the analysis process). Both grain size distributions follow a log-normal distribution except for the small grain size range where artifacts during processing of images render the analysis inconclusive.

average area of grains as a function of thermal annealing time for the PS−PI/d-PS 10 wt % blend system. The figure reveals that grain size rapidly increases after initiation of thermal annealing; however, it levels off after annealing times longer than 3 days. An analogous stagnation of grain growth was reported in Grain Coarsening-II for the PS−PI system admixed with a corresponding amount of hydrogenous PS.[48] There it was shown that grain stagnation results from the pinning of

DOI: 10.1021/acs.macromol.8b02044
Macromolecules 2018, 51, 10285−10296

GBs due to solute segregation.[48] The very similar results for both systems not only illustrate reproducibility but also confirm the assumption that the effect of PS solute on grain coarsening in PS−PI is independent of deuteration. As shown in the inset of Figure 5a, the increase of grain size is accompanied by the rapid relaxation of HAGBs after initiation of thermal annealing, eventually reaching a level state of $\phi_{HAGB} \sim 0.027$ (where the volume fraction has been calculated using stereology and assuming a GB thickness of L; see the Supporting Information). As will be shown below, the stagnation of HAGB content can be attributed to the segregation of d-PS solute within GB regions. Grain size distributions in as-cast (Figure 5b) and thermal annealed systems (Figure 5c) can be described by a log-normal distribution as is typical for systems undergoing "normal grain growth".[62,63] The occurrence of a log-normal grain size distribution after 7 days of thermal annealing is worthwhile noting because it might be expected that the "freezing-in" of HAGBs after ∼40 h of annealing (as seen in the inset of Figure 5a) might result in deviations from normal grain growth. The result implies that the pinning of HAGBs freezes grain coarsening as a whole, a conclusion that is also supported by the data shown in Figure 5a.

While grain mapping provides insight into a wide range of microstructural features, the experimental process is not practical to produce a more detailed temporal resolution or to provide information about the distribution of homopolymer solute within the copolymer matrix. For this purpose, a combined small- and ultrasmall-angle neutron scattering (SANS/USANS) analysis of the PS−PI/d-PS system was performed. It is important to note the different information that is contributed by the scattering data in the ultrasmall and small-angle range. USANS experiments extended over the range of the scattering vector 3×10^{-5} Å^{-1} < q < 2.5×10^{-3} Å^{-1}, thus yielding information about the structure on a length scale $d_s \sim 2\pi/q \approx 0.2$—20 μm, which is comparable to the dimension of GB interfaces. In contrast, the scattering of PS−PI/d-PS lamellae is expected to not contribute to the q dependence in this regime since $Lq_{USANS} \ll 1$.

To perform invariant analysis, the combined q range of USANS and SANS was considered. Note that the application of eq 1 for two-phase system requires that (1) the system contains only two phases, (2) the boundary between the two phases be sharp, and (3) the scattering length density of each phase is uniform. However, in real materials, inhomogeneities exist, for example, due to thermal density fluctuations and/or thermal concentration fluctuations—both are expected to contribute to the scattering at higher q. As our material system is in the solid state (measurements are being performed at room temperature), the scattering from thermal density fluctuation is assumed to be small compared to the contribution from concentration fluctuations. To correct for the scattering due to concentration fluctuations of d-PS, a correction method reported by Hashimoto and co-workers was applied (it is detailed in the Supporting Information).[64] As illustrated in Figure 6c, the effect of concentration fluctuations is most pronounced in the high-q range of the SANS data. The correction reveals the q^{-4} scaling of the scattering intensity that is indeed expected in the high-q range (Porod region).[64] For the purpose of invariant analysis, the scattering data were thus extrapolated according to q^{-2} and q^{-4} in the low- and high-q range.

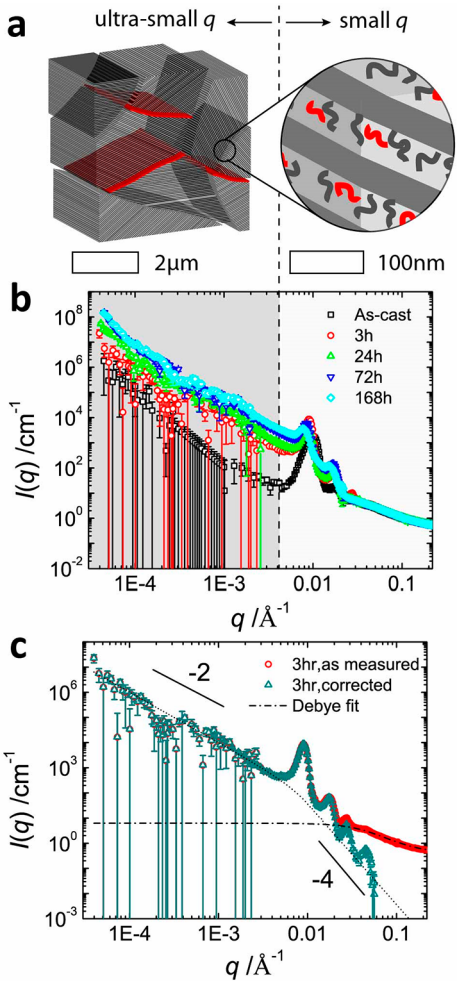

Figure 6. (a) Illustration of probe length scale of USANS and SANS along with the respective features of the microstructure giving rise to scattering. USANS scattering is due to grain-scale features such as HAGBs, while SANS scattering arises from the local lamellae structure. High-angle boundaries are highlighted in red to indicate selective segregation of d-PS solute. (b) Combined plots of USANS and SANS for PS−PI/d-PS 10 wt % after thermal annealing for 0, 3, 24, 72, and 168 h at T = 130 °C. The scattering intensity $I(q)$ in the USANS range increases by 3 orders of magnitude during thermal annealing. (c) Data for PS−PI/d-PS 10 wt % (annealing time is 3 h) after background correction (i.e., correction from scattering due to thermal concentration fluctuations). Also shown is the Debye model fit.

Using the extrapolated scattering data, we calculated the invariant via $Q = 4\pi\int q^2 I(q)\mathrm{d}q$, and subsequently the scattering contrast between HAGB regions and matrix, ΔSLD, was calculated according to eq 1. Figure 7 displays the evolution of ΔSLD as a function of annealing time of PS−PI/d-PS systems along with the corresponding invariant (shown in the inset of Figure 7). The low scattering strength of the as-cast system (which is orders of magnitude less than the corresponding value of annealed systems) confirms that ΔSLD is minimal in the as-cast state and strongly increases after initiation of thermal annealing to reach a final value of ΔSLD ≅ 2.5×10^{-6} Å^{-2} after about 40 h of annealing time. This supports the interpretation that the d-PS solute is initially uniformly distributed within the microstructure of as-cast films. Subsequently, during thermal annealing, d-PS rapidly diffuses into HAGB regions, thus resulting in the increase of scattering

DOI: 10.1021/acs.macromol.8b02044
Macromolecules 2018, 51, 10285−10296

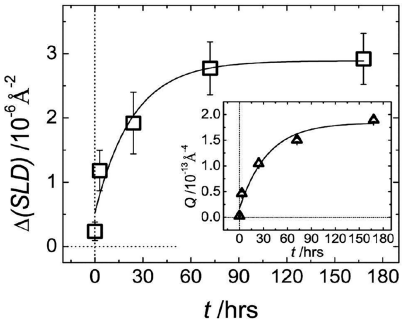

Figure 7. Plot of SLD contrast between HAGB regions and grain matrix as a function of thermal annealing time at T = 130 °C. The SLD contrast was calculated via eq 1 (see text for more details). The SLD contrast increases and saturates with thermal annealing due to segregation of d-PS solute within HAGB regions. The inset shows a plot of the invariant $Q = 4\pi\int q^2 I(q)\mathrm{d}q$ as a function of thermal annealing time (see text for more details). Lines are introduced to guide the eye.

contrast along HAGBs that saturates after annealing times of about 40 h once a limiting concentration of solute within HAGB regions has been reached.

To relate the experimental contrast in scattering length to the concentration of d-PS within HAGB regions several assumptions were made: first, the concentration of solute is uniform across all HAGBs; second, the thickness of HAGBs is equal to the lamellar spacing L independent of the amount of segregated d-PS; and third, the system can be represented as a two-phase material consisting of HAGB regions (partially filled with d-PS) and a uniform matrix with average scattering length density $\mathrm{SLD_m}$. With $\Delta\mathrm{SLD} = \mathrm{SLD_{HAGB}} - \mathrm{SLD_m}$ being known, the individual scattering length densities of boundary regions and grain matrix can then be determined to be a function of composition using eqs 2 and 3 as

$$\mathrm{SLD_{HAGB}} = \frac{x\nu}{\phi_{\mathrm{HAGB}}}\mathrm{SLD_{d\text{-}PS}} + \frac{\phi_{\mathrm{HAGB}} - x\nu}{\phi_{\mathrm{HAGB}}}\mathrm{SLD_{PS-PI}} \quad (2)$$

$$\mathrm{SLD_m} = \frac{(1-x)\nu}{1-\phi_{\mathrm{HAGB}}}\mathrm{SLD_{d\text{-}PS}} + \frac{1-\phi_{\mathrm{HAGB}} - (1-x)\nu}{1-\phi_{\mathrm{HAGB}}}\mathrm{SLD_{PS-PI}} \quad (3)$$

Here x denotes the relative fraction of d-PS that is segregated to the boundary (with respect to the total amount of added d-PS), ϕ_{HAGB} is the volume fraction of HAGBs, and ν is the total volume fraction of d-PS in the blend. Using these definitions, it can be seen that the terms $x\nu/\phi_{\mathrm{HAGB}}$ and $(\phi_{\mathrm{HAGB}} - x\nu)/\phi_{\mathrm{HAGB}}$ in eq 2 correspond to the respective volume fractions of d-PS and PS−PI in HAGB regions. Similarly, in eq 3 the term $(1-x)\nu/(1-\phi_{\mathrm{HAGB}})$ is the fraction of d-PS still present within the matrix, and $[(1-\phi_{\mathrm{HAGB}}) - (1-x)\nu]/(1-\phi_{\mathrm{HAGB}})$ is the volume fraction of PS−PI in the matrix. $\mathrm{SLD_{HAGB}}$ and $\mathrm{SLD_m}$ are therefore determined by the respective volume fractions of d-PS and PS−PI in the boundary and matrix regions and their respective scattering length densities ($\mathrm{SLD_{d\text{-}PS}} = 6.41 \times 10^{-6}$ Å^2 and $\mathrm{SLD_{PS-PI}} = 10^{-6}$ Å^2). With ϕ_{HAGB} being known from grain mapping analysis (see the inset in Figure 5a) and $\nu = 0.1$ being determined from the composition of the blend, the relative fraction x of d-PS solute that is segregated within HAGBs as well as the composition of HAGBs and matrix can be determined from the invariant analysis (via ΔSLD) through eqs 2 and 3. Figure 8 displays the evolution of the relevant compositional parameters during thermal annealing: the

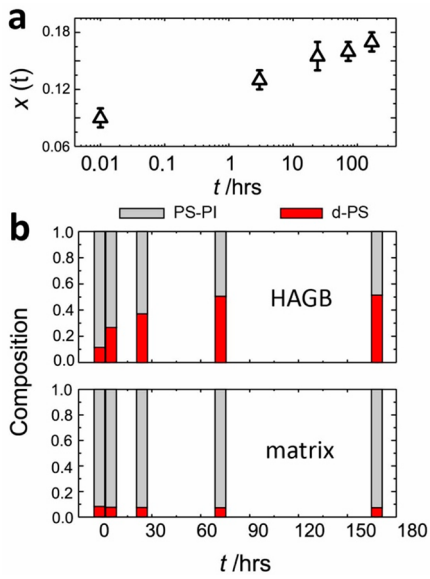

Figure 8. (a) Plot of the relative fraction of d-PS segregated to the boundary $x(t)$ as a function of time of thermal annealing at T = 130 °C. (b) Evolution of the composition of (top) HAGB and (bottom) matrix phase as a function of thermal annealing time. The red bar represents the volume fraction of d-PS solute (calculated via $x(t)\nu/\phi_{\mathrm{HAGB}}(t)$ for boundary regions and via $(1 - x(t))\nu/(1 - \phi_{\mathrm{HAGB}}(t))$ for the matrix), and the gray bar represents the respective volume fraction of PS−PI in both HAGB regions and matrix. Because HAGB regions represent only a small fraction of the total volume, the significant increase of the volume fraction of d-PS in HAGB regions during thermal annealing (from 0.12 at t = 0 to about a fraction of 0.52 at t = 168 h) is accompanied by only a modest decrease of the volume fraction of d-PS in the matrix (from 0.086 to about 0.075).

relative fraction of d-PS that has segregated within HAGB regions (see Figure 8a) and the composition or volume fraction of d-PS in HAGBs and the PS−PI matrix (see Figure 8b).

Several pertinent features should be highlighted from the data shown in Figure 8. First, the figure reveals that already in the as-cast state an imbalance in the distribution of d-PS exists. While a uniform distribution of d-PS would correspond to a volume fraction of 0.088, the respective volume fractions of d-PS in HAGBs and matrix in as-cast film are found to be 0.116 and 0.086. We attribute the modest accumulation of solute within HAGB regions of as-cast films to the accelerated dynamics during the late stages of solvent evaporation that enables some degree of solute diffusion. Note that the proximity of measured values to the expected value for uniform distribution also demonstrates the overall accuracy of the process used to determine the concentration of d-PS from ΔSLD. Second, thermal annealing initiates the rapid segregation and accumulation of d-PS within HAGB regions. After 3 h of annealing ∼14% of the added d-PS has segregated into HAGB regions (see Figure 8a) corresponding to a d-PS volume fraction of 0.25 within the boundary regions (see top panel in Figure 8b). The trend further suggests that after about 40 h of thermal annealing the concentration of d-PS in HAGB regions saturates at C_{HAGB} = 52 vol %. Because the overall volume fraction of HAGB regions is rather small ($\phi_{\mathrm{HAGB}} = 0.07$ in the as-cast state; see the inset in Figure 5a), the accumulation of d-PS within HAGBs has only a minor effect on the volume fraction of solute within the matrix which is

DOI: 10.1021/acs.macromol.8b02044
Macromolecules 2018, 51, 10285−10296

found to decrease from 0.086 (at t = 0) to a final value of 0.075.

To understand the driving force for solute segregation, Figure 9 displays the evolution of the relative GB surface

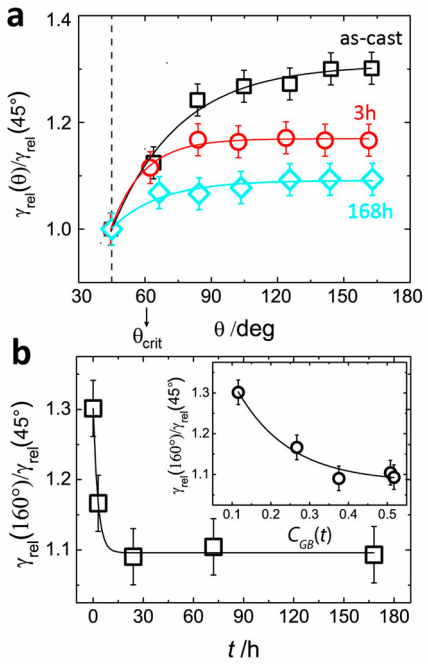

Figure 9. (a) Plot of relative GB tensions as a function of tilt angle after 0, 3, and 168 h of thermal annealing in PS−PI/d-PS (10 wt %). Grain boundary energy is normalized to respective values at θ = 45° (see text for more details). Thermal annealing decreases the relative GB tension of high angle boundaries by 16%. (b) Relative GB tension at tilt angle 160° normalized by that of the longest annealed system. The relative GB tension of high angle boundaries decreases rapidly with thermal annealing. Inset shows plot of the relative GB tension at θ = 160° normalized by $\gamma_{rel}(\theta = 45°)$ as a function of the volume fraction d-PS ($x\nu/\phi_{HAGB}$) in HAGB. The relative surface tension of HAGBs decreases with increasing accumulation of d-PS.

tension γ_{rel} of symmetric tilt boundaries during thermal annealing that was determined by analysis of dihedral angles of GB triple junctions (details on the experimental process are provided in ref 43).[43] Figure 9a displays the dependence of the relative GB energy on the misorientation (i.e., the tilt angle) for the PS−PI/d-PS system after 0, 3, and 168 h of thermal annealing. Note that GB energies are normalized with respect to the respective value at tilt angle θ = 45°, which was chosen because for $\theta < \theta_{crit}$ = 60° no solute segregation was observed, and hence GB energy should not be affected by thermal annealing. Consistent with previous reports, the GB energy increases with tilt angle and levels off at $\theta \cong$ 85° due to a transition in GB structure—this transition and its impact on $\gamma_{rel}(\theta)$ have been discussed in detail in Grain Coarsening-I.[47] A pertinent feature of the results shown in Figure 9a is the reduction of the relative energy of HAGBs during thermal annealing—the reduction reaches about 30% at θ = 160°. Interestingly, the evolution of the fractional GB tension $\gamma_{rel}(160°)/\gamma_{rel}(\theta = 45°)$ shown in Figure 9b reveals that the majority of the energetic stabilization of HAGBs occurs within the first 24 h of thermal annealing.

The inset in Figure 9b reveals that the decrease of the relative GB energy with thermal annealing correlates with the accumulation of d-PS in HAGB regions. Maximum stabilization is observed after 168 h of thermal annealing, i.e., when d-PS reaches a saturation volume fraction of 0.52. This presents—to the authors' knowledge—the first direct experimental correlation between solute segregation and GB energy. We hypothesize that the stabilization originates from the release of stored elastic strain energy that is caused by the relaxation of perturbed copolymer chains in the boundary region upon solute segregation. This implies that the extent and kinetics of solute segregation should be linked to the strain energy content of HAGB interfaces. To test this hypothesis, a statistical adsorption model was adopted to predict the rate of segregation as a function of GB energy.

Langmuir−McLean Model To Describe Solute Segregation in Lamellar Block Copolymer Systems. To better understand the kinetics of d-PS segregation within HAGB regions of the PS−PI/d-PS microstructure as well as the limiting concentrations of solute within matrix and boundary regions, we follow the approach by McLean.[65,66] McLean's model is commonly described as an extension of Langmuir's isotherm model to predict the segregation of foreign atoms within grain boundary regions in metal alloys. Specifically, the equilibrium composition of a system undergoing segregation of a solute is given by

$$\frac{X_{GB}}{1 - X_{GB}} = \frac{X_m}{1 - X_m} \exp\left[-\frac{\Delta E}{RT}\right] \quad (4)$$

where X_{GB} is the fraction of GB area decorated with solute, X_m is the overall concentration of solute in the matrix, and ΔE denotes the energy change associated with the segregation of solutes (which—in the case of solid solutions—is attributed to the release of stored elastic strain energy).[65,66] For the PS−PI/d-PS system in this study, we identify X_{GB} with the volume fraction of HAGB that is decorated with d-PS ($X_{GB} = x\nu/\phi_{HAGB}$) and X_m with the total filling fraction of d-PS ($X_m = \nu$) in the material. To apply eq 4, ΔE needs to be known as a function of grain misorientation (i.e., tilt angle) across the boundary. A process for calculating the absolute energy of tilt GBs in PS−PI has been reported on the basis of self-consistent field theory (SCFT); however, the simulation is limited to systems in the weak segregation regime, and hence the results cannot be directly applied to the present case.[41] Because of the absence of suitable simulation results, the GB energy was estimated using a continuum layer deformation model. The process used to estimate the energy of tilt boundaries will be briefly outlined in the following.

To estimate the energy change ΔE associated with the segregation of d-PS into HAGB regions, we assume that the energy change is equal to the elastic strain energy E_{el} that is released when solute accumulates in the boundary region and allows (PS) chains within the boundary region (that are perturbed from equilibrium) to resume their equilibrium conformation. We assume that the relaxation process is "complete"; i.e., the perturbed chains return to their full equilibrium conformation upon segregation of the solute. The omission of other contributions such as interface energy between microdomains is motivated by the observation that the microstructure of tilt GBs is not significantly altered upon solute segregation, and hence the total surface energy associated with the intermaterial dividing surface (IMDS) should remain about constant. The net energy gain upon relaxation of one PS chain in the boundary is thus estimated as

DOI: 10.1021/acs.macromol.8b02044
Macromolecules 2018, 51, 10285−10296

$3k_BT(h^2 - R_e^2)/(2R_e^2)$ where $R_e = n_{PS}^{1/2}l_{PS}$ is the equilibrium end-to-end distance (n_{PS} = 62.5 is the number of Kuhn segments per PS chain and l_{PS} = 18 Å is the Kuhn segment length) and h is the end-to-end distance (or brush height) of perturbed chains in the GB region.[67] It is further assumed that $h \approx R_e$ for lamellae in equilibrium. The dependence of the brush height h on the tilt angle can be evaluated using a geometric approach first introduced by Gido et al., who analyzed the energetics of symmetric tilt GB formation using a continuum mechanical model.[36] The approach evaluates the effect of boundary formation on chain conformation by analyzing the deformation of a two-dimensional slice through a volume element parallel to the IMDS that is subject to a bending deformation corresponding to a given tilt angle as illustrated in Figure 10a. The deformation is assumed to be affine and thus the end-to-end distance (or brush height) of chains within the GB region can be determined by evaluating the deformation of the slice. The approach starts out by relating the interface area $\Sigma(z)$ of the 2D slice at height z from the IMDS to the chain surface area per junction Σ_0 at the IMDS via $\Sigma(z) = (1 + 2Hz)\Sigma_0$ where $H = 1/(2R)$ is the mean curvature of the IMDS in the boundary. The latter is related to the boundary width W and the tilt angle via $R = W/(2\sin(\theta/2))$. Assuming that the polymer is incompressible and recalling that $W = L$ (see Figure 3), h and subsequently $E_{el}(\theta)$ can be determined to be a function of tilt angle—details of the procedure are provided in the Supporting Information. Figure 10 depicts the geometry used to estimate the brush height h and boundary energy $E_{el}(\theta)$ as well as the corresponding results of the analysis.

The elastic strain energy $E_{el}(\theta)$ can be related to the GB surface tension via $\gamma_{GB}(\theta) = E_{el}(\theta)/(N_{Av}\Sigma_0(\theta))$ which is shown in the inset of Figure 10c. The result reveals that boundary tension is in the "mJ/m^2" range and thus about 2 orders of magnitude less than corresponding values in metals or ceramics (a reflection of the entropic origin of the boundary tension in block copolymers). The predicted trend of $\gamma_{GB}(\theta)$ is in qualitative agreement with the experimental result (adopted from ref 43) that is shown as red line in the inset of in Figure 10c, albeit it is noted that the model underestimates (overestimates) estimates $d\gamma_{GB}(\theta)/d\theta$ in the range of small (large) misorientations. This is attributed to the transition of the GB structure from Chevron to Omega morphology which is not considered in the layer-deformation model. The values for $E_{el}(\theta)$ that were determined using the geometric model are within an order of magnitude of earlier SCFT results for the surface energy of tilt GBs in weakly segregated PS−PI. For example, Matsen reported for a symmetric PS−PI with degree of segregation χN = 20 at θ = 85° a surface energy of $E_{GB} \approx$ 1.4 kJ/mol, whereas our model yields $E_{el} \approx$ 7.7 kJ/mol.[41] We attribute the difference to the higher segregation strength in our systems that is expected to raise the boundary tension.[41] Because the relative boundary tension remains constant for $\theta >$ 85° (due to the Chevron/Omega transition; see Figure 9), we use in the following $E_{el}(\theta = 85°) = \Delta E = -7.7$ kJ/mol as a reference value for the energy change associated with solute segregation into HAGB regions. The negative sign is introduced to indicate that the energy is released upon solute segregation. By use of eq 4, the limiting filling fraction of d-PS within the boundary is predicted to be $x\nu/\phi \approx$ 0.49, in excellent agreement with the experimental value 0.52 that is determined by neutron scattering analysis (see Figure 8).

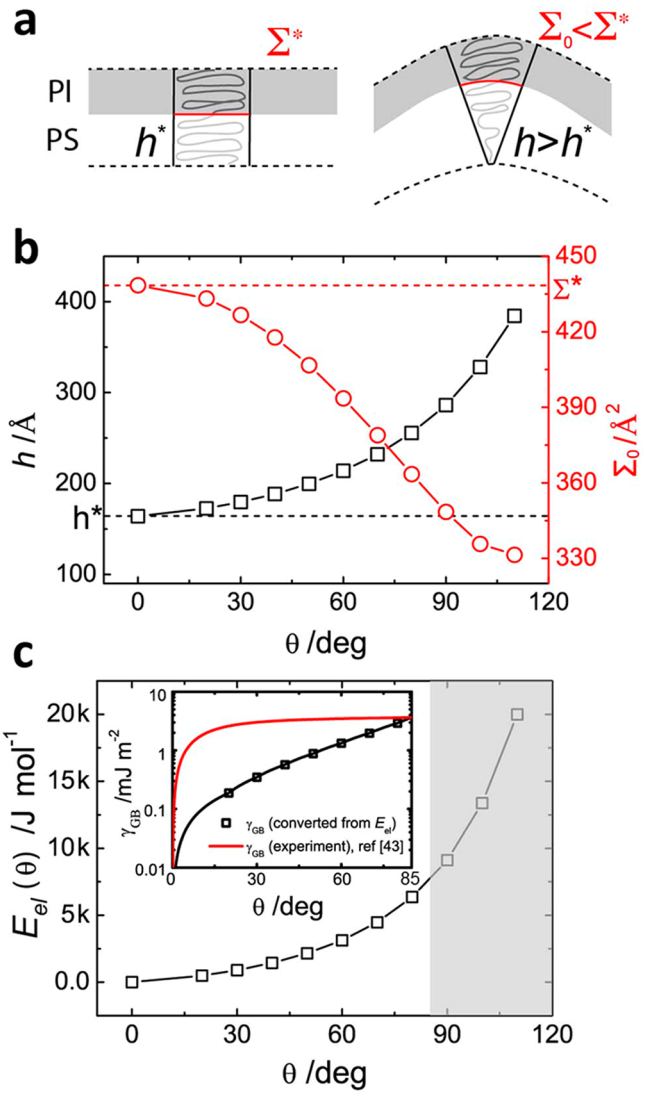

Figure 10. (a) Illustration of geometry used to evaluate the brush height h as a function of tilt angle. The chain on the concave part of the IMDS stretches and the area per chain Σ_0 decreases. (b) Dependence of the brush height h (concave side) and area per chain as a function of tilt angle. (c) Dependence of elastic strain energy $E_{el}(\theta)$ on the tilt angle determined based on $3/2(k_BT)(h^2 - R_e^2)/R_e^2$. Inset shows the corresponding dependence of grain boundary tension on title angle along with the corresponding experimental trend of $\gamma_{rel}(\theta)$ (red line; see text for more details). Highlighted in gray are misorientations that are not observed experimentally due to the transition from Chevron to Omega boundary morphology.

Similar to the boundary segregation isotherm, the kinetics of the segregation process can be evaluated if the energetic driving force ΔE as well as the mobility of the constituents are known. Specifically, the McLean result for the rate of solute accumulation in GB regions is given as

$$\frac{C_{GB}(t) - C_{GB}(0)}{C_{GB}(t_{max}) - C_{GB}(0)} = 1 - \exp[Bt]\,\mathrm{erfc}[\sqrt{Bt}] \quad (5)$$

where t_{max} is the time for reaching steady state and $B = 4D\alpha^{-2}W^{-2}$ with D denoting the diffusion constant of the d-PS and α = 6.8 denotes the ratio of d-PS concentration in GB regions after and before the annealing process (i.e., $x(t)\nu/\phi_{HAGB}(t)$ at $t = \infty$ and $t = 0$).[66] Figure 11 depicts the

DOI: 10.1021/acs.macromol.8b02044
Macromolecules 2018, 51, 10285−10296

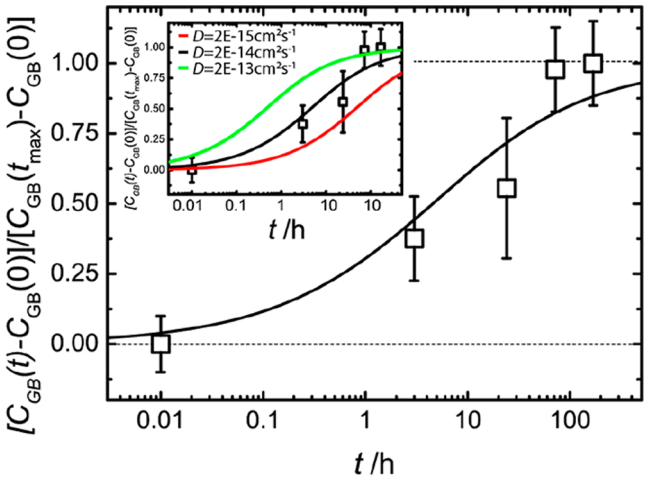

Figure 11. Plot of the normalized d-PS accumulation rate $[C_{GB}(t) - C_{GB}(0)]/[C_{GB}(\infty) - C_{GB}(0)]$ within HAGB regions as a function of thermal annealing time for PS−PI/d-PS samples annealed at T = 130 °C (here the subscript "GB" is used instead of "HAGB" for convenience). The solid line presents the predicted segregation rate calculated on the basis of a modified McLean model. The excellent agreement between experimental and predicted segregation rate supports that solute (d-PS) segregation is driven by the associated reduction of stored elastic energy in HAGB regions (see text for more details). The inset shows the predicted dependence of the segregation rate on the diffusivity of the solute that was calculated using eq 5. Distinct curves correspond to $D = 2 \times 10^{-15}$ cm^2 s^{-1} (red), 2×10^{-14} cm^2 s^{-1} (black), and 2×10^{-13} cm^2 s^{-1} (green).

normalized segregation rate $[C_{GB}(t) - C_{GB}(0)]/[C_{GB}(\infty) - C_{GB}(0)]$ that was determined by USANS/SANS analysis (square symbols) along with the predicted trend for solute accumulation in boundaries using eq 5 (solid line). The only unknown in eq 5 is the diffusion constant D that was determined by fitting of the model to the experimental data. The value inferred from the fit ($D \approx 2 \times 10^{-14}$ cm^2/s) is in excellent agreement with experimental results for a very similar material system reported by Lodge and co-workers.[68]

Several pertinent features in Figure 11 should be highlighted. First, the excellent agreement between the predicted and experimental trend for the rate of d-PS segregation (for reasonable values of the diffusion constant) supports the adequacy of the presented model to capture both the kinetics and energetics of d-PS segregation in PS−PI/d-PS blends. Second, model and experiment reveal that solute segregation occurs during the early stage of thermal annealing; for the particular case of PS−PI/d-PS, 50% of the solute is segregated within the first 5 h of thermal annealing. The most important governing parameter determining the segregation kinetics is expected to be the diffusion constant D of the solute which is sensitive to the molecular weight. The inset in Figure 11 displays the predicted influence of D on the solute accumulation rate that was calculated based on eq 5. For low molecular compounds with $D \approx 2 \times 10^{-13}$ cm^2 s^{-1}, segregation within only minutes of thermal annealing is expected. Also implied by eq 5 is that the rate of solute accumulation increases with the elastic strain energy that is released upon solute segregation, although the effect is less pronounced (result not shown here). It is noted that these predictions neglect any effect of "enthalpy of mixing" between solute and matrix and therefore are only adequate for athermal blends such as PS−PI/PS. The role of solute−matrix interactions on GB segregation is subject of our current research.

CONCLUSIONS

The segregation of solute additives (or impurities) into grain boundary regions within granular microstructures is a ubiquitous phenomenon in structured materials and often found to determine both the microstructure and properties that are attained through thermal processing of materials. However, while solute segregation is commonly associated with crystalline materials (where it is driven by the strong energy penalty associated with the incorporation of foreign atoms in a host lattice), our results reveal that the segregation of additives is also prominent in amorphous block copolymer/homopolymer blend systems in which "structure" occurs on the mesoscale. Segregation of the solute is limited to grain boundaries having misorientations exceeding a threshold value; the distribution of solute within these "high-angle boundaries" is approximately uniform and rapidly increases during thermal annealing. For the particular case of a lamellar PS−PI/d-PS blend, an ultimate d-PS volume fraction of 0.52 in the boundary regions is observed after 10 h of thermal annealing at T = 130 °C. The extent and kinetics of solute accumulation within high angle boundary regions can be quantitatively described using a Langmuir−McLean-type isotherm model that attributes the partitioning of the solute to the release of stored elastic strain energy as perturbed chains within the boundary region resume their equilibrium conformation. The model suggests that the segregation rate is primarily determined by the mobility of solute in the matrix while the limiting concentration of solute depends on the amount of stored elastic strain energy. We hope that our results will contribute to the better understanding of microstructure evolution in granular block copolymer materials in the presence of impurities (such as residual solvent or terminated chains) or purposefully added fillers (such has in the case of hybrid materials). The dense filling of boundary regions with additives might furthermore present opportunities for the design of novel functional materials in which networks of suitably decorated high-angle boundaries serve as "percolating path" to enable desired transport properties.

ASSOCIATED CONTENT

Supporting Information

The Supporting Information is available free of charge on the ACS Publications website at DOI: 10.1021/acs.macromol.8b02044.

Summary of materials characteristics; details of the stereological process for determining grain boundary volume fraction from electron micrographs; background correction process for neutron scattering data in the SANS regime; and detailed discussion of the continuous layer deformation model (PDF)

AUTHOR INFORMATION

Corresponding Author

*E-mail: bockstaller@cmu.edu.

ORCID

Michael R. Bockstaller: 0000-0001-9046-9539

DOI: 10.1021/acs.macromol.8b02044
Macromolecules 2018, 51, 10285−10296

Present Address

B.L.: Department of Chemical Engineering and Materials Science, Minneapolis, MN 55455-0431.

Notes

The authors declare no competing financial interest.

■ ACKNOWLEDGMENTS

This work was primarily supported by the National Science Foundation via Grants DMR-1410845 and DMR-1709344. M.R.B. further acknowledges support by the Department of Energy via Award DE-SC0018784. Access to USANS BT5 and NGB30SANS was provided by the Center for High Resolution Neutron Scattering, a partnership between the National Institute of Standards and Technology and the National Science Foundation under Agreement DMR-1508249. The authors acknowledge use of the Materials Characterization Facilities at Carnegie Mellon University supported by Grant MCF-678085.

■ REFERENCES

(1) Warren, S. C.; Messina, L. C.; Slaughter, L. S.; Kamperman, M.; Zhou, Q.; Gruner, S. M.; DiSalvo, F. J.; Wiesner, U. Ordered Mesoporous Materials from Metal Nanoparticle-Block Copolymer Self-Assembly. *Science* **2008**, *320* (5884), 1748−1752.

(2) Yoon, J.; Park, C.; Thomas, E. L. Enabling Nanotechnology with Self Assembled Block Copolymer Patterns. *Polymer* **2003**, *44* (22), 6725−6760.

(3) Kang, Y.; Walish, J. J.; Gorishnyy, T.; Thomas, E. L. Broad-Wavelength-Range Chemically Tunable Block-Copolymer Photonic Gels. *Nat. Mater.* **2007**, *6* (12), 957−960.

(4) Fink, Y.; Urbas, a. M.; Bawendi, M. G.; Joannopoulos, J. D.; Thomas, E. L. Block Copolymers as Photonic Bandgap Materials. *J. Lightwave Technol.* **1999**, *17* (11), 1963−1969.

(5) Crossland, E. J. W.; Kamperman, M.; Nedelcu, M.; Ducati, C.; Wiesner, U.; Smilgies, D.-M.; Toombes, G. E. S.; Hillmyer, M. A.; Ludwigs, S.; Steiner, U.; et al. A Bicontinuous Double Gyroid Hybrid Solar Cell. *Nano Lett.* **2009**, *9* (8), 2807−2812.

(6) Bockstaller, M. R.; Thomas, E. L. Optical Properties of Polymer-Based Photonic Nanocomposite Materials. *J. Phys. Chem. B* **2003**, *107* (37), 10017−10024.

(7) Bockstaller, M. R.; Mickiewicz, R. A.; Thomas, E. L. Block Copolymer Nanocomposites: Perspectives for Tailored Functional Materials. *Adv. Mater.* **2005**, *17* (11), 1331−1349.

(8) Bockstaller, M.; Kolb, R.; Thomas, E. L. Metallodielectric Photonic Crystals Based on Diblock Copolymers. *Adv. Mater.* **2001**, *13* (23), 1783−1786.

(9) Ullal, C. K.; Maldovan, M.; Thomas, E. L.; Chen, G.; Han, Y.-J.; Yang, S. Photonic Crystals through Holographic Lithography: Simple Cubic, Diamond-like, and Gyroid-like Structures. *Appl. Phys. Lett.* **2004**, *84* (26), 5434.

(10) Maldovan, M.; Thomas, E. L. Diamond-Structured Photonic Crystals. *Nat. Mater.* **2004**, *3* (9), 593−600.

(11) Bates, C. M.; Maher, M. J.; Janes, D. W.; Ellison, C. J.; Willson, C. G. Block Copolymer Lithography. *Macromolecules* **2014**, *47* (1), 2−12.

(12) Wu, M. L.; Wang, D.; Wan, L. J. Directed Block Copolymer Self-Assembly Implemented via Surface-Embedded Electrets. *Nat. Commun.* **2016**, *7*, 1−7.

(13) Hu, H.; Gopinadhan, M.; Osuji, C. O. Directed Self-Assembly of Block Copolymers: A Tutorial Review of Strategies for Enabling Nanotechnology with Soft Matter. *Soft Matter* **2014**, *10* (22), 3867−3889.

(14) Mansky, P.; DeRouchey, J.; Russell, T. P.; Mays, J.; Pitsikalis, M.; Morkved, T.; Jaeger, H. Large-Area Domain Alignment in Block Copolymer Thin Films Using Electric Fields. *Macromolecules* **1998**, *31* (13), 4399−4401.

(15) Olszowka, V.; Hund, M.; Kuntermann, V.; Scherdel, S.; Tsarkova, L.; Böker, A. Electric Field Alignment of a Block Copolymer Nanopattern: Direct Observation of the Microscopic Mechanism. *ACS Nano* **2009**, *3* (5), 1091−1096.

(16) Rokhlenko, Y.; Majewski, P. W.; Larson, S. R.; Gopalan, P.; Yager, K. G.; Osuji, C. O. Implications of Grain Size Variation in Magnetic Field Alignment of Block Copolymer Blends. *ACS Macro Lett.* **2017**, *6* (4), 404−409.

(17) Segalman, R. A.; Yokoyama, H.; Kramer, E. J. Graphoepitaxy of Spherical Domain Block Copolymer Films. *Adv. Mater.* **2001**, *13* (15), 1152−1155.

(18) Li, M.; Ober, C. K. Block Copolymer Patterns and Templates. *Mater. Today* **2006**, *9* (9), 30−39.

(19) Ruiz, R.; Kang, H.; Detcheverry, F. A.; Dobisz, E.; et al. Density Multiplication and Improved Lithography by Directed Block Copolymer Assembly. *Science (Washington, DC, U. S.)* **2008**, *321*, 936−939.

(20) Stoykovich, M. P.; Mueller, M.; Kim, S. O.; Solak, H. H.; Edwards, E. W.; De Pablo, J. J.; Nealey, P. F. Directed Self-Assembly of Block Copolymer Blends into Nonregular Device-Oriented Structures. *Science (Washington, DC, U. S.)* **2005**, *308*, 1442−1446.

(21) Amundson, K.; Helfand, E.; Quan, X.; Hudson, S. D.; Smith, S. D. Alignment of Lamellar Block Copolymer Microstructure in an Electric Field. 2. Mechanisms of Alignment. *Macromolecules* **1994**, *27* (22), 6559−6570.

(22) Qiang, Z.; Zhang, Y.; Groff, J. A.; Cavicchi, K. A.; Vogt, B. D. A Generalized Method for Alignment of Block Copolymer Films: Solvent Vapor Annealing with Soft Shear. *Soft Matter* **2014**, *10* (32), 6068−6076.

(23) Goveas, J. L.; Milner, S. T. Dynamics of the Lamellar-Cylindrical Transition in Weakly Segregated Diblock Copolymer Melts. *Macromolecules* **1997**, *30* (9), 2605−2612.

(24) Dai, H.; Balsara, N.; Garetz, B.; Newstein, M. Grain Growth and Defect Annihilation in Block Copolymers. *Phys. Rev. Lett.* **1996**, *77* (17), 3677−3680.

(25) Chastek, T. Q.; Lodge, T. P. Grain Shapes and Growth Kinetics during Self-Assembly of Block Copolymers. *J. Polym. Sci., Part B: Polym. Phys.* **2006**, *44* (3), 481−491.

(26) Heinzer, M. J.; Han, S.; Pople, J. A.; Baird, D. G.; Martin, S. M. In Situ Tracking of Domain Growth During the Drying of Solution-Cast Block Copolymer Films Using Small Angle X-Ray Scattering: Ordering Kinetics. *Macromolecules* **2012**, *45*, 3480.

(27) Garetz, B. A.; Balsara, N. P.; Dai, H. J.; Wang, Z.; Newstein, M. C.; Majumdar, B. Orientation Correlations in Lamellar Block Copolymers. *Macromolecules* **1996**, *29* (1), 4675−4679.

(28) Newstein, M. C.; Garetz, B. A.; Balsara, N. P.; Chang, M. Y.; Dai, H. J. Growth of Grains and Correlated Grain Clusters in a Block Copolymer Melt. *Macromolecules* **1998**, *31* (1), 64−76.

(29) Kim, W. G.; Chang, M. Y.; Garetz, B. A.; Newstein, M. C.; Balsara, N. P.; Lee, J. H.; Hahn, H.; Patel, S. S. Effect of Quench Depth on Grain Structure in Quiescently Ordered Block Copolymers. *J. Chem. Phys.* **2001**, *114* (22), 10196−10211.

(30) Kim, W. G.; Garetz, B. A.; Newstein, M. C.; Balsara, N. P. Maximizing the Grain Growth Rate during the Disorder-to-Order Transition in Block Copolymer Melts. *J. Polym. Sci., Part B: Polym. Phys.* **2001**, *39* (19), 2231−2242.

(31) Chang, M. Y.; Abuzaina, F. M.; Kim, W. G.; Gupton, J. P.; Garetz, B. A.; Newstein, M. C.; Balsara, N. P.; Yang, L.; Gido, S. P.; Cohen, R. E.; et al. Analysis of Grain Structure in Partially Ordered Block Copolymers by Depolarized Light Scattering and Transmission Electron Microscopy. *Macromolecules* **2002**, *35* (11), 4437−4447.

(32) Balsara, N. P.; Marques, C. M.; Garetz, B. A.; Newstein, M. C.; Gido, S. P. Anisotropy of Lamellar Block Copolymer Grains. *Phys. Rev. E: Stat. Phys., Plasmas, Fluids, Relat. Interdiscip. Top.* **2002**, *66*, 052802.

(33) Chastek, T. Q.; Lodge, T. P. Grain Shapes and Growth Kinetics of the Cylinder Phase in a Block Copolymer Solution. *Macromolecules* **2004**, *37* (13), 4891−4899.

DOI: 10.1021/acs.macromol.8b02044
Macromolecules 2018, 51, 10285−10296

(34) Chastek, T. Q.; Lodge, T. P. Twinning and Growth Kinetics of Lamellar Grains in a Diblock Copolymer Solution. *J. Polym. Sci., Part B: Polym. Phys.* **2005**, *43* (4), 405−412.
(35) Gido, S. P.; Thomas, E. L. Lamellar Diblock Copolymer Grain Boundary Morphology. 2. Scherk Twist Boundary Energy Calculations. *Macromolecules* **1994**, *27* (3), 849−861.
(36) Gido, S. P.; Gunther, J.; Thomas, E. L.; Hoffman, D. Lamellar diblock copolymer grain boundary morphology. 1. Twist boundary characterization. *Macromolecules* **1993**, *26*, 4506.
(37) Gido, S. P.; Thomas, E. L. Lamellar Diblock Copolymer Grain Boundary Morphology. 3. Helicoid Section Twist Boundary Energy. *Macromolecules* **1997**, *30*, 3739−3746.
(38) Gido, S. P.; Schwark, D. W.; Thomas, E. L.; do Carmo Goncalves, M. Observation of a Non-Constant Mean Curvature Interface in an ABC Triblock Copolymer. *Macromolecules* **1993**, *26*, 2636−2640.
(39) Nishikawa, Y.; Kawada, H.; Hasegawa, H.; Hashimoto, T. Grain Boundary Morphology of Lamellar Microdomains. *Acta Polym.* **1993**, *44* (5), 247−255.
(40) The terminology "twist" and "tilt" refers to the underlying deformation mode of an ideal lamellar bicrystal structure that gives rise to the grain boundary: tilt-GBs involve a rotation between adjacent grains about an axis in the plane of the grain boundary while for twist boundaries the axis of rotation is normal to the boundary.
(41) Matsen, M. W. Kink Grain Boundaries in a Block Copolymer Lamellar Phase. *J. Chem. Phys.* **1997**, *107* (19), 8110−8119.
(42) Duque, D.; Katsov, K.; Schick, M. Theory of T Junctions and Symmetric Tilt Grain Boundaries in Pure and Mixed Polymer Systems. *J. Chem. Phys.* **2002**, *117* (22), 10315.
(43) Ryu, H. J.; Fortner, D. B.; Rohrer, G. S.; Bockstaller, M. R. Measuring Relative Grain-Boundary Energies in Block Copolymer Microstructures. *Phys. Rev. Lett.* **2012**, *108* (10), 1−5.
(44) Burgaz, E.; Gido, S. P. T-Junction Grain Boundaries in Block Copolymer - Homopolymer Blends. *Macromolecules* **2000**, *33*, 8739−8745.
(45) Gaines, M. K.; Smith, S. D.; Samseth, J.; Bockstaller, M. R.; Thompson, R. B.; Rasmussen, K. Ø.; Spontak, R. J. Nanoparticle-Regulated Phase Behavior of Ordered Block Copolymers. *Soft Matter* **2008**, *4* (8), 1609.
(46) Thompson, R. B. Tilt Grain Boundaries in a Diblock Copolymer Ordered Nanocomposite Lamellar Phase. *J. Chem. Phys.* **2010**, *133* (14), 144902 1−5. .
(47) Ryu, H. J.; Fortner, D. B.; Lee, S.; Ferebee, R.; De Graef, M.; Misichronis, K.; Avgeropoulos, A.; Bockstaller, M. R. Role of Grain Boundary Defects during Grain Coarsening of Lamellar Block Copolymers. *Macromolecules* **2013**, *46* (1), 204−215.
(48) Ryu, H. J.; Sun, J.; Avgeropoulos, A.; Bockstaller, M. R. Retardation of Grain Growth and Grain Boundary Pinning in Athermal Block Copolymer Blend Systems. *Macromolecules* **2014**, *47* (4), 1419−1427.
(49) Kline, S. R. Reduction and Analysis of SANS and USANS Data using Igor Pro. *J. Appl. Crystallogr.* **2006**, *39* (6), 895.
(50) Glinka, C. J.; Barker, J. G.; Hammouda, B.; Krueger, S.; Moyer, J. J.; Orts, W. J. The 30 m Small-Angle Neutron Scattering Instruments at the National Institute of Standards and Technology. *J. Appl. Crystallogr.* **1998**, *31* (3), 430.
(51) Barker, J. G.; Glinka, C. J.; Moyer, J. J.; Kim, M. H.; Drews, A. R.; Agamalian, M. Design and performance of a thermal-neutron double-crystal diffractometer for USANS at NIST. *J. Appl. Crystallogr.* **2005**, *38* (6), 1004.
(52) Eitouni, H. B.; Balsara, N. P. *Thermodynamics of Polymer Blends, Physical Properties of Polymer Handbook*, 2nd ed.; Mark, J. E., Ed.; Springer: 2006.
(53) Sears, V. F. Neutron scattering lengths and cross sections. *Neutron News* **1992**, *3* (3), 26−37.
(54) Listak, J.; Bockstaller, M. R. Stabilization of Grain Boundary Morphologies in Lamellar Block Copolymer/Nanoparticle Blends Stabilization of Grain Boundary Morphologies in Lamellar Block Copolymer/Nanoparticle Blends. *Macromolecules* **2006**, *39*, 5820−5825.
(55) Myers, R. T.; Cohen, R. E.; Bellare, A. Use of Ultra-Small-Angle X-Ray Scattering To Measure Grain Size of Lamellar Styrene - Butadiene Block Copolymers. *Macromolecules* **1999**, *32*, 2706−2711.
(56) Brust, M.; Walker, M.; Bethell, D.; Schiffrin, D. J.; Whyman, R. Synthesis of Thiol-Derivatised Gold Nanoparticles in a Two-Phase Liquid-Liquid System. *J. Chem. Soc., Chem. Commun.* **1994**, *0*, 801−802.
(57) Jia, X.; Listak, J.; Witherspoon, V.; Kalu, E. E.; Yang, X.; Bockstaller, M. R. Effect of Matrix Molecular Weight on the Coarsening Mechanism of Polymer-Grafted Gold Nanocrystals. *Langmuir* **2010**, *26* (14), 12190−12197.
(58) Listak, J.; Hakem, I. F.; Ryu, H.-J.; Rangou, S.; Politakos, N.; Misichronis, K.; Avgeropoulos, A.; Bockstaller, M. R. Effect of Chain Architecture on the Compatibility of Block Copolymer/Nanoparticle Blends. *Macromolecules* **2009**, *42* (15), 5766−5773.
(59) The prevalence of tilt boundaries within lamellar block copolymer microstructures has been reported before and can be attributed to the lower energy of this boundary type as well as the influence of mechanical stresses during film formation. See also refs 60 and 61.
(60) Netz, R. R.; Andelman, D.; Schick, M. Interfaces of Modulated Phases. *Phys. Rev. Lett.* **1997**, *79*, 1058−1061.
(61) Gido, S. P.; Thomas, E. L. Lamellar Diblock Copolymer Grain Boundary Morphology. 4. *Macromolecules* **1994**, *27*, 6137−6144.
(62) Burke, J. E.; Turnbull, D. Recrystallization and Grain Growth. *Prog. Met. Phys.* **1952**, *3*, 220−292.
(63) Humphreys, F. J.; Hatherly, M. *Recrystallization and Related Annealing Phenomena*, 2nd ed.; Oxford: UK, 2004.
(64) Koizumi, S.; Hasegawa, H.; Hashimoto, T. Spatial Distribution of Homopolymers in Block Copolymer Microdomains As Observed by a Combined SANS and SAXS Method. *Macromolecules* **1994**, *27* (26), 7893−7906.
(65) Lejcek, P. *Grain Boundary Segregation in Metals*; Springer: 2010.
(66) McLean, D. *Grain Boundaries in Metals*; Oxford: 1957.
(67) Rubinstein, M.; Colby, Ralph, H. *Polymer Physics*; Oxford: 2003.
(68) Eastman, C. E.; Lodge, T. P. Self-Diffusion and Tracer Diffusion in Styrene/2-Vinylpyridine Block Copolymer Melts. *Macromolecules* **1994**, *27*, 5591−5598.

DOI: 10.1021/acs.macromol.8b02044
Macromolecules 2018, 51, 10285−10296